Ensemble Forecasting for the Gulf of Mexico Loop Current Region

Patrick J. Haley, Jr.[a], Chris Mirabito[a], Manan Doshi[a], Pierre F. J. Lermusiaux[a, †]
[a] *Department of Mechanical Engineering, Massachusetts Institute of Technology, Cambridge, MA*
[†]Corresponding author: pierrel@mit.edu

***Abstract*—In recent years, the Gulf of Mexico Loop Current System has received increased attention. Its dynamics and the warm water it transports from the Caribbean influence the local weather and ecosystems. The high velocities of the Loop Current and the eddies it sheds can disrupt important industries. Accurate forecasting of the Loop Current system is challenging, in part because of the lack of data over long enough periods of time, which leads to considerable uncertainty. In this work, we describe and apply our MIT Multidisciplinary Simulation, Estimation, and Assimilation Systems (MSEAS) and Error Subspace Statistical Estimation (ESSE) ensemble forecasting methodology and software to estimate such uncertainty and to inform data collection in a quantitative manner. The ensemble forecasts allow for mitigating risks and optimizing data collection. We demonstrate that our probabilistic system has qualitative skill for over a month. We show that uncertainty grows along and around the Loop Current and its eddies, and transfers to depth from the shelf and slope. Using information theory, we find that our probabilistic hindcasts can have predictive capabilities for one to three months, with a slower loss of predictability in the quieter Loop Current states. Through the use of correlation and mutual information fields, we optimize future sampling by predicting the impacts and information content of observations. We find that the most informative data are those that either directly sample dynamically relevant areas or sample coastal modes that are correlated with these areas. Subsurface data are shown to have more impact on forecasts of one month or longer.**

***Index Terms*—ocean modeling, probabilistic forecasting, predictability, skill, adaptive sampling, mutual information.**

I. Introduction

In the Gulf of Mexico (GoM), the strength of hurricanes, the health of coastal and estuarine ecosystems, the exploration and extraction of oil and gas, the fishing industry, and ultimately the region's economy as a whole are heavily influenced by the location and dynamics of the Loop Current (LC) [1–3]. The LC is a warm-water current that flows northward from the Caribbean Sea, protrudes into the GoM, and exits through the Florida Strait. The degree to which the LC penetrates the GoM is highly variable. The northernmost extent of the penetration has a range of $24°$N to $28°$N [4–7]. This penetration has been observed to have a bimodal distribution [4, 7–15]. The major mode of this distribution is centered on $26.5°$N to $26.75°$N, with the minor mode centered on $24.5°$N to $24.75°$N. The horizontal extent of this penetration is also highly variable in time, but has been observed to exhibit quasi-periodic behavior, with the minimum penetration generally occurring in January, peak intensification and penetration growth occurring during the springtime months (February to May), and maximum penetration occurring in July [8, 9, 15]. However, it is not only the location of the LC, but also its sporadic and episodic shedding of long-lived LC Eddies (LCE) that often disrupt local ecosystems and industrial operations at sea in the northern, central, and western GoM [1, 7, 13, 14, 16–22].

The desire to better understand and forecast the highly variable LC system has driven much modeling work. This includes both isolated hindcasts and forecasts [5, 10, 11, 13, 15, 23–31] as well as extended forecasting operations [32–40]. The limited availability of data for these forecasting operations has led in turn to large uncertainties in long-range model forecasts of the LC and LCE locations and dynamics. Moreover, the impact of these limited observations on such forecasts has been challenging to ascertain in a rigorous, quantitative manner, and remains an important question in the scientific community.

Thus, the overarching goals of this work are to showcase principled methods and systems for (i) estimating forecast uncertainties, and (ii) informing data collection so as to maximize the impact of the data on longer forecasts. To start addressing these goals, we (i) employ large (200- to 500-member) ensemble hindcasts from our MIT Multidisciplinary Simulation, Estimation, and Assimilation Systems primitive equation (MSEAS-PE) and Error Subspace Statistical Estimation (ESSE) software to initialize and hindcast uncertainties and (ii) utilize these ensemble hindcasts to estimate the statistics and probability density functions (pdf) needed to compute predictive capabilities, predictability limits, and data impact using correlations and mutual information (MI) fields.

The remainder of this paper is organized as follows. In section II, we outline our overall forecasting methodology, including a description of OUR probabilistic ocean modeling system. We also briefly describe the statistical tools we use to quantify predictability and data impact. Next, in section III, we showcase the results of our deterministic hindcasts, and provide a brief skill assessment. In section IV, we present our probabilistic hindcasts, describe the evolution of the uncertainty, and discuss the predictability limits. We discuss applications of our ensemble hindcasts to optimal sampling strategies in section V. Finally, conclusions are in section VI.

II. Methodology

For the probabilistic ocean simulations, we employ our MIT MSEAS-PE and ESSE systems [41–45]. These systems have been used for fundamental research and for realistic simulations in varied regions of the World Ocean [46–52]. Among the many strengths and capabilities of the MSEAS-PE is its ability to simulate (sub-)mesoscale processes over regional domains with complex geometries and varied interactions using an implicit two-way nesting/tiling scheme [41]. We

979-8-218-14218-6 ©2023 MTS

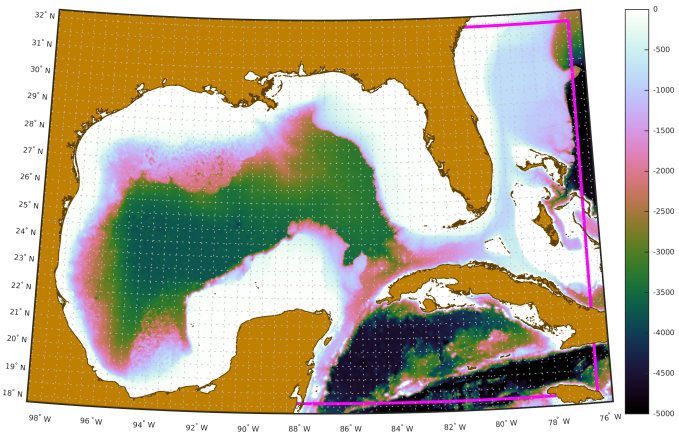

Fig. 1: MSEAS-PE GoM modeling domain and bathymetry.

leverage many of our systems' capabilities, including deterministic and ensemble initialization schemes [42, 53, 54], tidal prediction and inversion [55], fast-marching coastal objective analysis [56], subgrid-scale models [57, 58], advanced data assimilation schemes [59, 60], and path planning and adaptive sampling [48, 60–62].

Deterministic modeling. We set up our multi-resolution MSEAS-PE modeling system in the following manner. We utilized the bathymetry from the Shuttle Radar Topography Mission (SRTM) 15-arcsecond global map [63–65], plus the NOAA 3-arcsecond bathymetry for the shelf and slope, to construct a combination of tiling and telescoping implicit two-way nested domains, with $1/12.5°$, $1/25°$, $1/50°$ and $1/100°$ horizontal resolution, and with 100 optimized vertical levels (fig. 1). The model is forced with tides from TPXO8-Atlas data from OSU [66, 67], adapted to the high-resolution bathymetry and coastlines [55], and is atmospherically forced with hourly $1/5°$ Climate Forecast System (CFS) output from NCEP [68]. The sub-tidal initial and boundary conditions are downscaled from the HYbrid Coordinate Ocean Model (HYCOM) [69, 70], with optimized velocities for high-resolution coasts and bathymetry [42].

ESSE ensemble hindcasts. We set up our ESSE ensemble and data assimilation in the following manner. The ensemble is atmospherically forced with an ensemble of products from NCEP and ECMWF (namely $1/5°$ CFS, $1/4°$ GFS, and $1/4°$ ERA5) [71–73]. The sub-tidal initial and boundary conditions are downscaled from four different models: the combined HYCOM and MITgcm [74], the Regional Ocean Modeling System (ROMS) [75], and the Nucleus for European Modelling of the Ocean (NEMO) [76]. We initialize large ESSE hindcast ensembles [58, 60, 77] of 200 to 500 members with perturbed initial conditions, boundary conditions, and stochastic forcing [58, 78, 79]. To create 3D PE-balanced initial ESSE perturbations, we used historical CTD profiles (2008–2018) from the World Ocean Database [80], which we quality-controlled and segregated into four water masses (see fig. 2). We then computed 1D vertical empirical modes for each region. These vertical modes were combined with 2D horizontal modes created by an eigendecomposition of the horizontal correlation matrix (100 km decay scale, 250 km zero-crossing) to produce 3D temperature and salinity modes based on each region [53, 54]. Perturbations of magnitude equal to a fraction of this variability were constructed from these modes. They were combined based on the fronts of the deterministic ICs to create 3D temperature and salinity perturbations for the entire domain. Initial perturbations for sea surface height (SSH) and velocity were obtained through geostrophy. Finally, the ensemble fields were initialized at least 4 days in advance of the first time of interest to allow PE adjustments. Each ensemble used one to three different atmospheric forecasts with perturbed amplitudes and phases, up to around 10 central barotropic tidal forcings with perturbed amplitudes and phases, and perturbed model parameters.

Correlation fields. Upon completion of the ensemble hindcasts, we utilize the output to compute ESSE correlation hindcasts among the field of interest and candidate observations (location, type, and sampling platforms). For each period and platform type, we forecast the correlation C_{XY} between a candidate observed variable X at one point at the initial time, and each point of a whole field Y at a given (future) verification time (e.g., 0, 30, 60, or 90 days later). To obtain a single overall value of a correlation field, we compute the Gulf-area-averaged correlation C, summing over only those

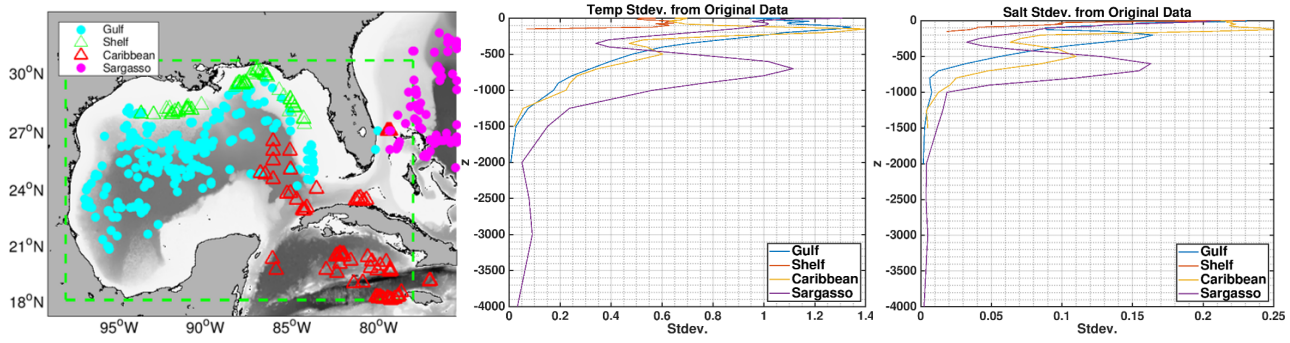

(a) Historical data locations (b) Temperature standard deviation profiles (c) Salinity standard deviation profiles

Fig. 2: Locations and standard deviation profiles of historical in situ data, segregated by water mass, used to construct 3D modes for 3D PE-balanced ESSE perturbations. Shown here are historical April data, used for simulations in the 2015 period.

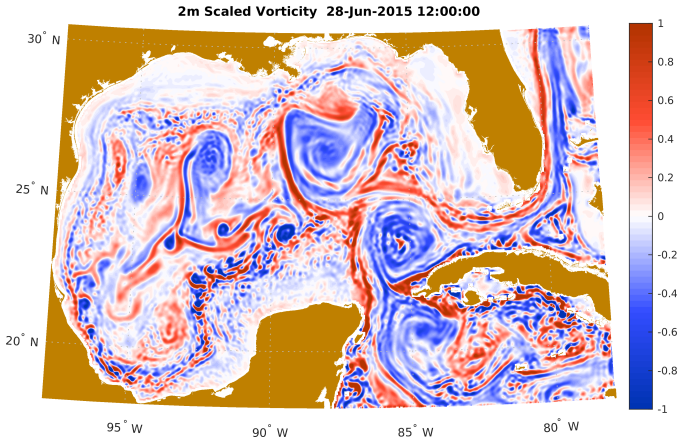

Fig. 3: Scaled-vorticity at 2 m depth of a $1/25°$-resolution MSEAS-PE hindcast for June 28, 2015 at 12:00Z.

areas where $|C_{XY}| \geq 0.2$. Since some platforms can measure multiple variables at multiple depths, we then average C over all such variables and depths to obtain a single value $\langle C \rangle$ for a given candidate point and verification time. We repeat this process for each candidate data point, and compare the values of $\langle C \rangle$ across all candidate points to determine the most valuable observation points.

MI fields. Finally, for principled estimation of optimal data types, platforms, and locations, we consider mutual information (MI) [81]. MI provides a rigorous information-theoretic foundation for this estimation, while correlation provides an aid in interpretation and a sanity check of MI estimates. MI measures how much information about random variables is obtained by observations of other random variables. The MI between two scalar or vector variables is defined as

$$\mathrm{MI}(X,Y) = H(X) - H(X|Y) = H(Y) - H(Y|X)\,, \quad (1)$$

where H denotes the entropy of the distribution.

III. Deterministic Results: LC States Forecasting Skill

We examine different states of the LC system: (1) retracted (the LC "hugs" Cuba and does not penetrate far into the GoM); (2) extended (the LC penetrates further north into the GoM before turning south and exiting through the Florida Strait); (3) either of the previous states with LCEs present [1, 82]. The MSEAS-PE model was run for 1 to 3 months during three different periods: 2011, 2012–2013, and 2015, chosen for their different LC states. During June–September 2011, the LC is extended with a large LCE separation. During December 2012–January 2013, the LC is transitioning from a long retracted state to an extended state. Finally, the May–June 2015 period is in the middle of a period of LC hyperactivity [19]: The remnants of eddies *Lazarus* and *Michael* are decaying in the western GoM. The eddy *Nautilus* detaches from the LC and splits off a second eddy *Nautilus II*. By late June eddy *Olympus* is shed from the LC.

An example of a $1/25°$-resolution deterministic, hindcast of 2 m scaled-vorticity for June 28, 2015 is shown in figure 3. The vorticity clearly highlights the LC in its extended state while it is undergoing an eddy shedding/separation event. It also reflects the presence of the eddies *Nautilus*, *Nautilus II*, and *Olympus*. Finer-scale features are present along the shelf break as well, particularly along Campeche Bank and at the Louisiana–Texas shelf.

A qualitative evaluation of the MSEAS-PE hindcast skill is made by comparing the SSH field gradients predicted by MSEAS-PE with those output from NOAA AOML/CoastWatch [83] for the 2012–2013 and 2015 periods; these are shown in figure 4. In both periods, there is a broad qualitative agreement of the SSH gradients, and there is agreement between the hindcasts and the LC states. The simulated positions of main features are accurate throughout these one-month periods. Note, however, that there are some differences in the 2015 period in the coastal regions near the

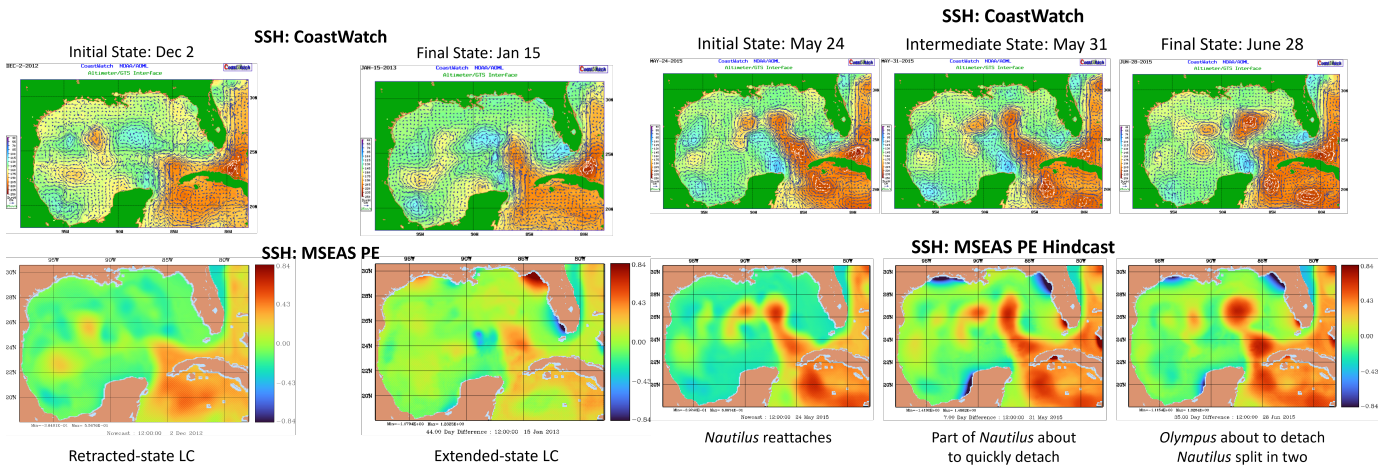

(a) December 2, 2012 to January 15, 2013

(b) May 24 to June 28, 2015

Fig. 4: Comparison of MSEAS-PE hindcast SSH fields with the data-based NOAA AOML/CoastWatch analyses.

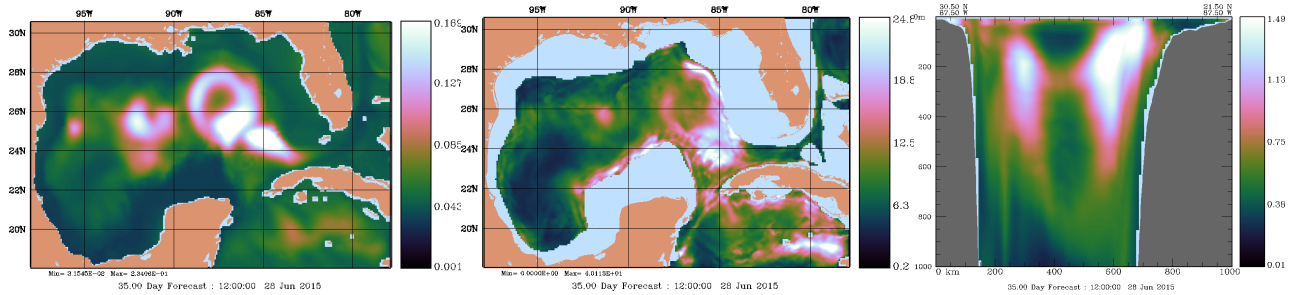

(a) Surface elevation (b) 500 m velocity magnitude (c) Temperature section along 87.5°W

Fig. 5: ESSE ensemble standard deviations: 35-day hindcast fields for June 28, 2015.

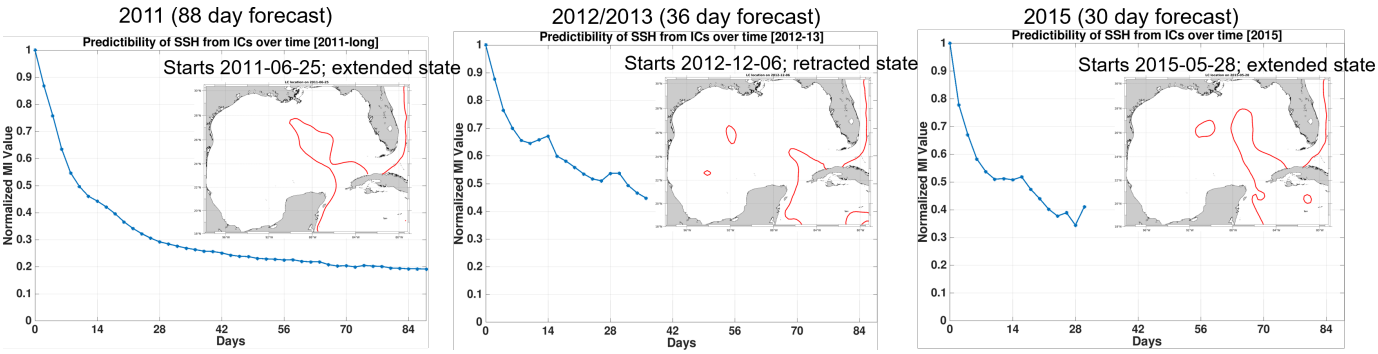

Fig. 6: ESSE ensemble hindcasts of predictability. Shown is the predicted time series of relative mutual information between the initial SSH field and future SSH fields for the 2011, 2012–2013, and 2015 modeling periods. The insets show the initial state of the LC.

Yucatán peninsula, Louisiana, and northwestern Florida, likely from tidal effects not included in CoastWatch but present in the MSEAS-PE simulations. Overall, the underlying deterministic hindcasts have skill by predicting LC state changes, such as a ring separation in 2015, one month in advance.

IV. Probabilistic Results: Uncertainty and Predictability Forecasts

With reasonable skill demonstrated by the deterministic hindcasts, we proceed with the ensemble hindcasts that simulate uncertainties due to initial conditions, boundary conditions, and stochastic atmospheric and tidal forcing. We first examine the evolution of uncertainty fields. Figure 5 shows the ensemble standard deviation of the SSH and 500 m velocity fields and of the temperature field in a north-south section along 87.5°W. In the 2015 ensemble, the dynamic response to the stochastic tidal forcing quickly introduces a baseline uncertainty of about 3 cm in SSH over the entire domain (see fig. 5a). Larger uncertainty (15 to 25 cm) develops around the LCE and northeast edge of the LC (in an area unconstrained by the LCE). A weak tidal response alternately increases and decreases the SSH uncertainty by the northwest coast of Florida. Looking deeper at the 500 m velocity (shown in fig. 5b), we see larger uncertainty (15 to 25 cm/s) develop around the LCE, in the LC region constrained by topography and along the topographic slopes. The uncertainty evolves over the simulation period, first being confined to the continental shelves and slope (not shown), and then propagating to the deep waters closer to the center of the Gulf; this is shown in figure 5c, with the effect being especially prevalent off the north slope of Campeche Bank.

We see similar evolution of the uncertainty in the 2011 and 2012–2013 ensembles. One notable difference is in the SSH uncertainty. Since this is a transition to an extended LC state with no LCE, the larger uncertainty in the LC extends further westward to the upstream side of the extension as far back as to where the LC is constrained by the Campeche Bank.

We next demonstrate our principled ensemble hindcasts of predictability limits for these modeling periods. To determine how much information about the future hindcast SSH is in the initial SSH, we use the pdfs from our large ensemble ESSE hindcasts and compute the MI between the initial and final SSH states. The results are shown in figure 6 where time-series of relative MI are drawn for each of the 3 periods. For the 2011 period, we find that by day 90 the MI retains 20% of its original value after about 3 months and is still decreasing (i.e., the MI has not yet reached its asymptotic value). This indicates that the SSH predictability limit is approximately 3 months.

Our results also quantitatively confirm that this predictability limit varies with the initial state of LC system. Notably, both the 2011 and 2015 ensembles start in an extended state with LCE shedding occurring during the simulations. The MI in both cases drops to 50% of its initial value by day 10. However, for the 2012–2013 ensemble, which starts in a retracted state and transitions to an extended state, the MI does not drop to 50% of its initial value until day 26. Finally,

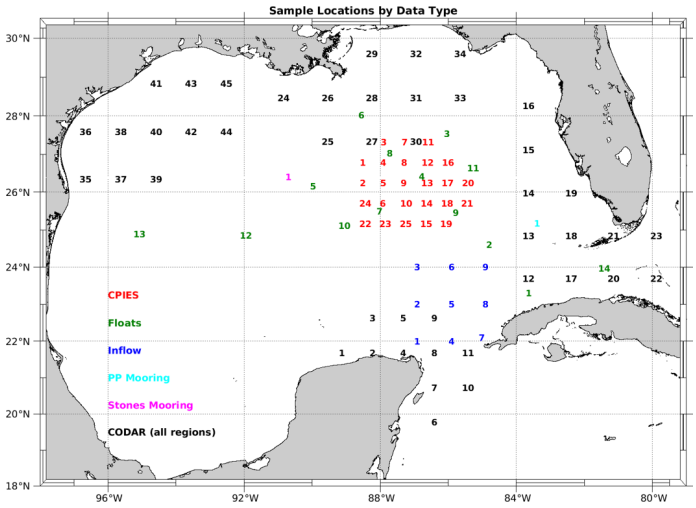

Fig. 7: Candidate measurement types and locations considered (numbered and colored by type) for each candidate observation platform.

we note that the predictability limit would be longer if we assumed perfect atmospheric forecasts, but here we account for atmospheric forecast uncertainty.

V. Sampling Results: Forecasting the Value of Observations

A major thrust of the present UGOS efforts is to employ principled observational campaign design strategies so as to answer the question of what, where and when to observe (now) to provide the most information for future forecasts [48, 79]. Our strategy is to use a combination of correlations and MI fields (computed using our ensemble hindcasts) to predict the information content and impacts of observations.

We first consider five observational platform types which were used by UGOS in recent sampling campaigns: (i) current- and pressure-recording inverted echo sounders (CPIES) [84], which measure subsurface T, S, u, and v (at multiple depths); (ii) autonomous profiling floats (such as Argo [85]; a subset of observing locations is considered here), which measure subsurface T and S; (iii) the West Florida Shelf pressure point mooring (located off the Dry Tortugas) [86], which measures subsurface T, S, u, and v; (iv) the Stones mooring [87], which measures subsurface currents; and (v) coastal ocean dynamics applications radar (CODAR), a land-based high frequency (HF) radar [88] that measures surface currents over a given region (a subset of points in four different sampling regions is considered here). To these locations we added a hypothetical inflow array (where the LC enters the GoM), which would measure subsurface T, S, u, and v. The set of all possible measurement locations for our study is shown in figure 7.

Correlation hindcasts for candidate scalar observations. We examine and compare candidate scalar sampling using correlations. For each period and observation platform, we hindcast correlations between one given scalar measured variable (at a particular location and depth) at the initial time with SSH at three verification times: the initial time, 14 days later, and 31 days later. A small subset of examples of the resulting correlation fields for the 2011 modeling period are shown in figure 8. For that period and LC state, we predict a strong correlation between the 500 m temperature at one of the CPIES locations near the downstream side of the extended LC and the SSH 31 days later, especially around the eastern sides of the LCE that breaks off and the remaining LC. A moderately strong correlation exists between the 500 m temperature at one of the float locations near the downstream side of the extended LC (a bit north of the CPIES location examined) and the SSH 31 days later around the east and west sides of the LCE. A weaker correlation exists between the 500 m velocity at the Stones mooring and the SSH 31 days later around the LCE. Similarly, we predict a weaker, spotty correlation between the 500 m temperature at the same CPIES location and the eddy kinetic energy (EKE) at 1300 m 31 days later, between the LC and the northeast shelf of the GoM.

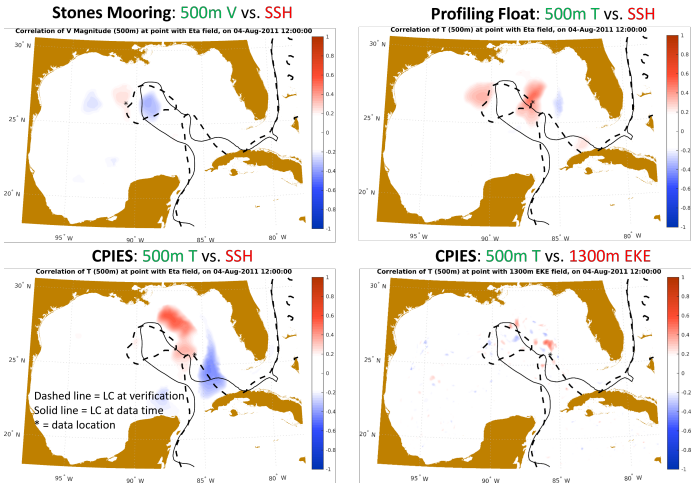

Fig. 8: MIT-MSEAS ESSE correlation hindcasts for the 2011 period. The target observation (green text) is made at the initial time; the verification field (red text) is 31 days later. The observation platform is indicated in **bold text** for each plot.

Averaged correlation hindcasts for candidate observations. To heuristically combine correlations between several observations and the later fields, we turn to the Gulf-area-averaged correlation ($\langle C \rangle$, §II). In figure 9 we show bar plots of $\langle C \rangle$ between data at each sampling point and SSH at 0, 14, and 31 days after the data sampling for each ensemble period. For all the periods, the CPIES and floats have the most correlation with the later SSH. We also see that correlations tend to be largest for the 2012–2013 period (retracted-to-extended state) and weakest for the 2015 period (hyperactive period). This is consistent with our earlier results on the decays of MI (fig. 6).

We next apply our ESSE correlation hindcasts to heuristically estimate the most valuable sampling locations for each of the three modeling periods. Figure 10 shows the values of $\langle C \rangle$ for each observation platform type and location for the 2015 modeling period. We note that there are three distinct types of observation locations with high correlation to the future SSH: (1) observations that directly sample the LC system dynamics; (2) observations that sample a coastal mode correlated to the

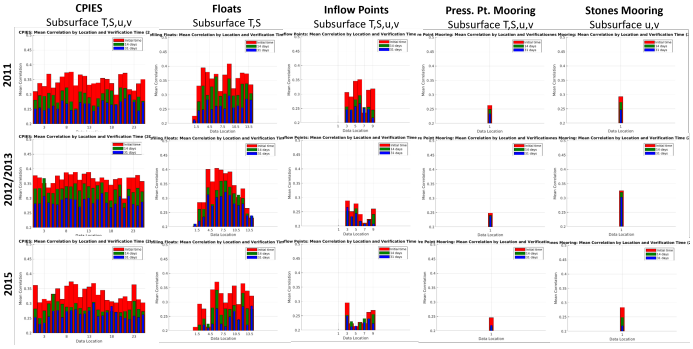

Fig. 9: Comparison of MIT-MSEAS ESSE $\langle C \rangle$ (predicted Gulf-area-averaged, variable and depth-averaged correlation with SSH) for each observation platform and location, verification time, and modeling period.

LC system; and (3) observations that sample both. During this time, the LC is in an extended state. Correlations predict that it is best to sample near the LC edges and between the LC and eddy *Nautilus* (sampling the interior of the LC was less important). Outlying high values of $\langle C \rangle$ in figure 10 correspond to high-correlation candidate observations of the second or third types. In contrast, in 2011, when the LC pinches, correlations predict that it is best to sample the base of LC and the inflow region (between the Yucatán peninsula and Cuba), as well as in the Florida Strait (not shown). Meanwhile, in 2012–2013, when the LC is in the retracted state, we predict it is best to sample close to the tip of the LC, as well as in the LC inflow region, and in the Florida Strait (also not shown). We remark that in all years, the most important observation locations are those that sample dynamically relevant areas or sample a coastal mode that is correlated with dynamically relevant areas; the observation type is somewhat less important.

MI forecasts for candidate multivariate vector observations. We now rigorously compare candidate sampling locations, types, and platforms using MI (eq. 1). An advantage of MI is that it naturally extends to multivariate, multi-point comparisons [48]. Figure 11 shows the predicted multivariate MI between candidate data sets and SSH 30 days later in the 2011 period. The top row shows the MI between two different CPIES locations and the SSH 30 days later. Unlike correlations, these MI values involve temperature, salinity, and velocity at multiple depths with the later SSH. The first CPIES point (along the downstream side of the LC) provides much information on the SSH along the downstream side of the later LC. The second CPIES point (more on the upstream side of the LC) provides less information on the LC, but the information it provides peaks around the location of the LCE. The bottom row shows another level of aggregation. The bottom left panel shows the multivariate MI between five CPIES locations (T, S, u, v at multiple depths) and SSH 30 days later. Here we see these CPIES locations provide good information concentrated around the downstream LC and the LCE. Finally, we examine the aggregate MI between surface velocity measured by the CODAR station in Florida to the SSH 30 days later. Here the MI field shows the information is more diffuse and highlights a coastal mode correlated with the LC.

To obtain a more global picture with MI we can simply aggregate futher and compute MI for all field points at the later time and rigorously compute the information that we obtained heuristically with the averaged $\langle C \rangle$. Figure 12 shows this globally computed MI between each type of data (all variables and depths) at the initial time and the fields (SSH or 1300 m EKE) at the initial time, 14 days, and 31 days later. Again, results confirm more information content in the quieter 2012–2013 period. Results also show that subsurface data (PIES, floats, the hypothetical inflow array, etc.) commonly have more impact on the combined SSH and 1300 m EKE hindcasts than surface-only data (e.g., CODAR) for hindcasts of one month or longer. The natural aggregation of the MI makes it easier to

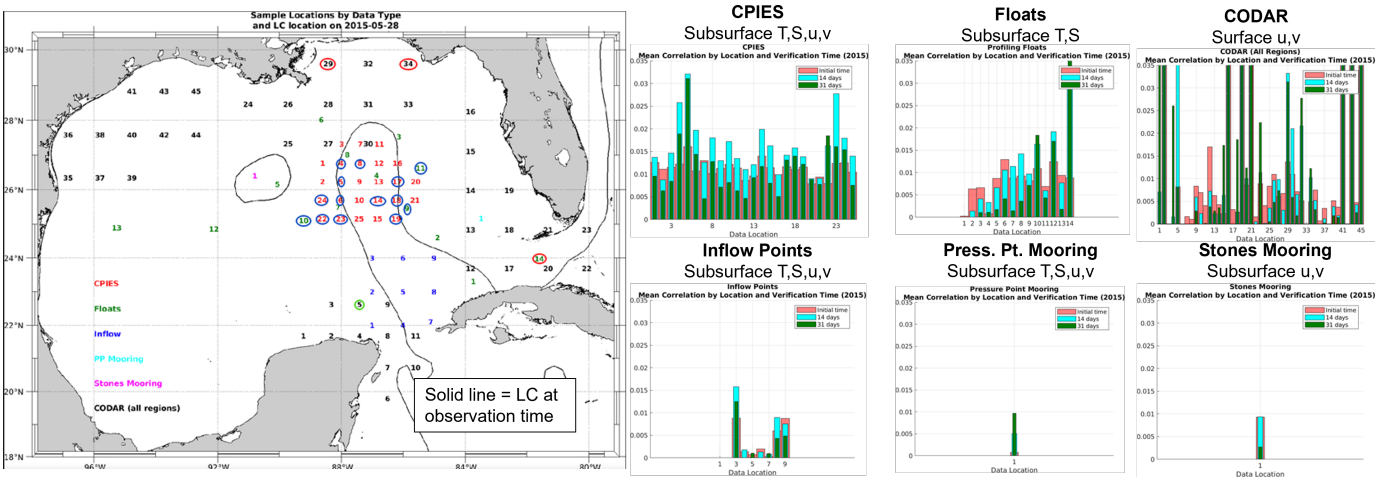

Fig. 10: Comparison of $\langle C \rangle$ for all platform types and locations, and verification times, based on the MIT-MSEAS ESSE correlation hindcasts for 2015. There are 3 distinct types of observation locations with high correlation to the future SSH: (1) observations that directly sample LC system dynamics (blue circles); (2) observations that sample a coastal mode correlated to the LC system (red circles); and (3) observations that sample both (green circles).

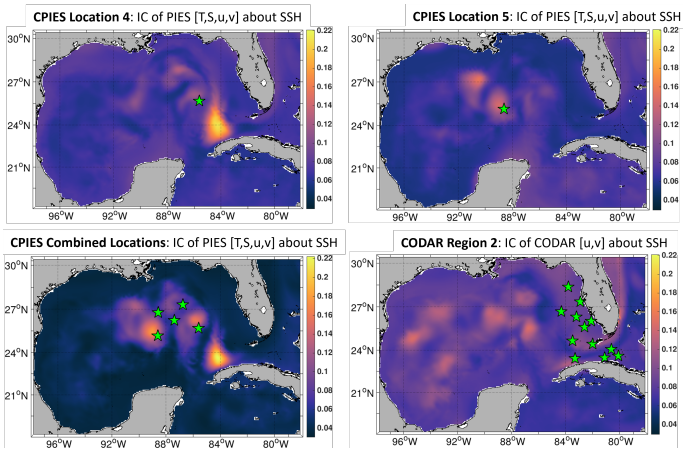

Fig. 11: MIT-MSEAS ESSE hindcasts of MI fields for the 2011 period. They predict MI between a candidate data set at an initial time and SSH 30 days later.

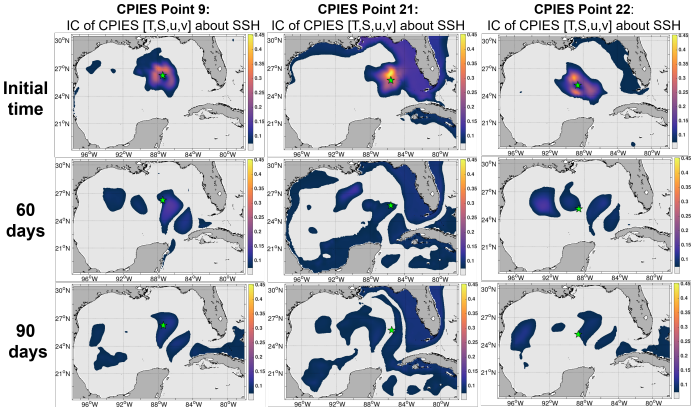

Fig. 13: Information content, for selected CPIES locations in 2011 containing T, S, u, and v, about SSH at the initial time, after 60 days, and after 90 days

predict the potential impact of the hypothetical inflow array.

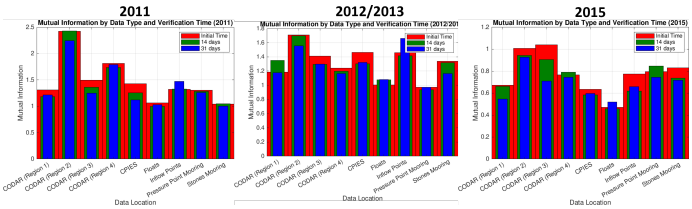

(a) Verification field: SSH

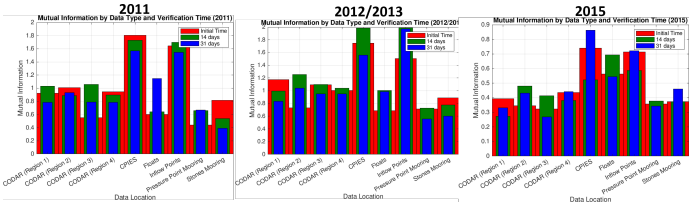

(b) Verification field: 1300 m EKE

Fig. 12: Comparison of the MIT-MSEAS ESSE hindcast MI with future SSH and 1300 m EKE for each observation platform, verification time, and modeling period.

Finally, we utilize the results of our 2011 ensemble hindcast to predict the information content about future SSH, given a set of CPIES locations containing [T, S, u, v] at the initial time. We wish to determine such information content at the initial time, as well as 60 days later (after the LCE separation event), and after 90 days. These relative MI fields are shown in figure 13. As expected, in accord with the LC system dynamics, the MI values decay over time. Notice that after 60 days, some MI peaks are still at 40-50% of their initial value, with the MI spreading. Some information (between 5% and 15% of the initial value) remains about SSH after 90 days, again as expected since we are approaching the predictability limit of the hindcasts, as discussed in section IV.

VI. Conclusion

In this paper, we developed and applied large-ensemble forecasting in the GoM using our MSEAS-PE modeling system and our ESSE scheme. We explained how to utilize the ensemble results to compute correlation and MI hindcasts. We ran one- to three-month-long deterministic hindcasts for three modeling periods, encompassing common LC configuration states and transitions. We demonstrated that these underlying deterministic hindcasts showed qualitative skill. We ran large-ensemble hindcasts for three time periods and discussed the evolution and propagation of uncertainty. Specifically, we found that the hindcasted uncertainty grows near the LC and eddies and that this uncertainty is transferred from the shelf and slope into the deep water. We estimated predictability limits by using the large ensemble ESSE hindcast pdfs to compute the principled MI between the initial and final SSH states, and found that significant predictability of SSH can reach one to three months or more, depending on the LC state. The decay of predictability when the LC was in the quieter, retracted state was slower than during more energetic states. To predict optimal sampling locations, times, and measurement variable(s), we ranked candidate data sets according to the information they provide about the future ocean state, using a combination of hindcasts of correlation and MI. For the periods studied, the most informative observation locations are those that sample dynamically relevant areas or sample coastal modes that are correlated with dynamically relevant areas. If the LC is in a retracted state, it is best to sample close to the tip of LC, in the LC inflow region, and in the Florida Strait. If it is in an extended state, it is best near the LC edges and between the LC and an eddy. If it is in an LCE separation event, it is best at the base of the LC, inflow region, and the Florida Strait. We also found that subsurface data commonly have more impact on hindcasts of one month or longer.

Our results can be useful for future studies and observation campaigns in the Gulf of Mexico. They can be used to determine the variables most relevant to LCE separation events, to guide possible future investments in instrumentation for near-real-time data collection, and to better inform the design of future short- and long-term campaigns.

ACKNOWLEDGMENTS

We thank all members of the MSEAS group, past and present. We are grateful to the Understanding Gulf Ocean Systems (UGOS) program of the National Academies of Sciences, Engineering, and Medicine, for partial research support under grant 2018-2798-03, to the Massachusetts Institute of Technology (MIT). We also thank all of our Gulf of Mexico colleagues. Finally, we thank the HYCOM team for their ocean fields, as well as NCEP and ECMWF for their atmospheric forcing forecasts and reanalyses. ERA5 data was downloaded from the Copernicus Climate Change Service (C3S) (2023).

REFERENCES

[1] The National Academy of Sciences, "Understanding Gulf ocean systems," 2018.

[2] M. Cadwaller, "Eddy lazarus & the loop current – paralyzing the gulf in 2014," American Association of Drilling Engineers: Innovative and Emerging Technology Study Group, January 2015.

[3] S. F. DiMarco, W. D. Nowlin, and R. Reid, "A statistical description of the velocity fields from upper ocean drifters in the gulf of mexico," *Geophysical Monograph-American Geophysical Union*, vol. 161, p. 101, 2005.

[4] A. Alvera-Azcárate, A. Barth, and R. H. Weisberg, "The surface circulation of the caribbean sea and the gulf of mexico as inferred from satellite altimetry," *Journal of Physical Oceanography*, vol. 39, no. 3, pp. 640 – 657, 2009.

[5] G. Gopalakrishnan, B. D. Cornuelle, I. Hoteit, D. L. Rudnick, and W. B. Owens, "State estimates and forecasts of the loop current in the gulf of mexico using the mitgcm and its adjoint," *Journal of Geophysical Research: Oceans*, vol. 118, no. 7, pp. 3292–3314, 2013.

[6] P. Hamilton, K. Donohue, C. Hall, R. Leben, H. Quian, J. Sheinbaum, and R. Watts, "Observations and dynamics of the Loop Current," US Department of the Interior, Bureau of Ocean Energy Management, Gulf of Mexico OCS Region, New Orleans, OCS Study BOEM 2015-006, 2014.

[7] X. Zeng, Y. Li, and R. He, "Predictability of the loop current variation and eddy shedding process in the gulf of mexico using an artificial neural network approach," *Journal of Atmospheric and Oceanic Technology*, vol. 32, no. 5, pp. 1098 – 1111, 2015.

[8] D. W. Behringer, R. L. Molinari, and J. F. Festa, "The variability of anticyclonic current patterns in the gulf of mexico," *Journal of Geophysical Research (1896-1977)*, vol. 82, no. 34, pp. 5469–5476, 1977.

[9] F. M. Vukovich, "Loop current boundary variations," *Journal of Geophysical Research: Oceans*, vol. 93, no. C12, pp. 15 585–15 591, 1988.

[10] G. Gopalakrishnan, B. D. Cornuelle, and I. Hoteit, "Adjoint sensitivity studies of loop current and eddy shedding in the gulf of mexico," *Journal of Geophysical Research: Oceans*, vol. 118, no. 7, pp. 3315–3335, 2013.

[11] D. S. Dukhovskoy, R. R. Leben, E. P. Chassignet, C. A. Hall, S. L. Morey, and R. Nedbor-Gross, "Characterization of the uncertainty of loop current metrics using a multidecadal numerical simulation and altimeter observations," *Deep Sea Research Part I: Oceanographic Research Papers*, vol. 100, pp. 140–158, 2015.

[12] J. Sheinbaum, G. Athié, J. Candela, J. Ochoa, and A. Romero-Arteaga, "Structure and variability of the yucatan and loop currents along the slope and shelf break of the yucatan channel and campeche bank," *Dynamics of Atmospheres and Oceans*, vol. 76, pp. 217–239, 2016, the Loop Current Dynamics Experiment.

[13] J. Jouanno, J. Ochoa, E. Pallàs-Sanz, J. Sheinbaum, F. Andrade-Canto, J. Candela, and J.-M. Molines, "Loop current frontal eddies: Formation along the campeche bank and impact of coastally trapped waves," *Journal of Physical Oceanography*, vol. 46, no. 11, pp. 3339 – 3363, 2016.

[14] H. Furey, A. Bower, P. Perez-Brunius, P. Hamilton, and R. Leben, "Deep eddies in the gulf of mexico observed with floats," *Journal of Physical Oceanography*, vol. 48, no. 11, pp. 2703 – 2719, 2018.

[15] A. Lugo-Fernández, "Modeling the intrusion of the loop current into the gulf of mexico," *Dynamics of Atmospheres and Oceans*, vol. 84, pp. 46–54, 2018.

[16] A. Lugo-Fernández and R. R. Leben, "On the linear relationship between loop current retreat latitude and eddy separation period," *Journal of Physical Oceanography*, vol. 40, no. 12, pp. 2778 – 2784, 2010.

[17] D. L. Rudnick, G. Gopalakrishnan, and B. D. Cornuelle, "Cyclonic eddies in the gulf of mexico: Observations by underwater gliders and simulations by numerical model," *Journal of Physical Oceanography*, vol. 45, no. 1, pp. 313 – 326, 2015.

[18] K. Donohue, D. Watts, P. Hamilton, R. Leben, M. Kennelly, and A. Lugo-Fernández, "Gulf of mexico loop current path variability," *Dynamics of Atmospheres and Oceans*, vol. 76, pp. 174–194, 2016, the Loop Current Dynamics Experiment.

[19] N. Sharma, J. S. Storie, K. M. Obenour, M. J. Leber, and A. Srinivasan, "Loop Current hyperactivity: Analysis of in situ measurements in the Gulf of Mexico," in *Offshore Technology Conference*, no. OTC-27229-MS. Houston: OnePetro, May 2016, pp. 1–30.

[20] P. Hamilton, A. Bower, H. Furey, R. Leben, and P. Pérez-Brunius, "The loop current: Observations of deep eddies and topographic waves," *Journal of Physical Oceanography*, vol. 49, no. 6, pp. 1463 – 1483, 2019.

[21] W. Sturges and R. Leben, "Frequency of ring separations from the loop current in the gulf of mexico: A revised estimate," *Journal of Physical Oceanography*, vol. 30, no. 7, pp. 1814 – 1819, 2000.

[22] A. R. Johnson, K. A. Donohue, D. R. Watts, K. L. Tracey, and M. A. Kennelly, "Generation of high-frequency topographic rossby waves in the gulf of mexico," *Frontiers in Marine Science*, vol. 9, 2022.

[23] H. E. Hurlburt and J. D. Thompson, "A numerical study of loop current intrusions and eddy shedding," *Journal of Physical Oceanography*, vol. 10, no. 10, pp. 1611 – 1651, 1980.

[24] L. Oey, T. Ezer, and H. Lee, "Loop current, rings and related circulation in the gulf of mexico: A review of numerical models and future challenges," in *Circulation in the Gulf of Mexico: Observations and Models*, ser. Geophysical Monograph, W. Sturges and A. Lugo-Fernandez, Eds. Washington, D.C.: AGU American Geophysical Union, 2005, vol. 161, pp. 31–56.

[25] L.-Y. Oey, T. Ezer, G. Forristall, C. Cooper, S. DiMarco, and S. Fan, "An exercise in forecasting loop current and eddy frontal positions in the gulf of mexico," *Geophysical Research Letters*, vol. 32, no. 12, 2005.

[26] I. Hoteit, T. Hoar, G. Gopalakrishnan, N. Collins, J. Anderson, B. Cornuelle, A. Köhl, and P. Heimbach, "A mitgcm/dart ensemble analysis and prediction system with application to the gulf of mexico," *Dynamics of Atmospheres and Oceans*, vol. 63, pp. 1–23, 2013.

[27] F.-H. Xu, L.-Y. Oey, Y. Miyazawa, and P. Hamilton, "Hindcasts and forecasts of loop current and eddies in the gulf of mexico using local ensemble transform kalman filter and optimum-interpolation assimilation schemes," *Ocean Modelling*, vol. 69, pp. 22–38, 2013.

[28] J. Jouanno, E. Pallàs-Sanz, and J. Sheinbaum, "Variability and dynamics of the yucatan upwelling: High-resolution simulations," *Journal of Geophysical Research: Oceans*, vol. 123,

no. 2, pp. 1251–1262, 2018.

[29] K. Chen, R. He, B. S. Powell, G. G. Gawarkiewicz, A. M. Moore, and H. G. Arango, "Data assimilative modeling investigation of gulf stream warm core ring interaction with continental shelf and slope circulation," *Journal of Geophysical Research: Oceans*, vol. 119, no. 9, pp. 5968–5991, 2014.

[30] S. L. Morey, J. Zavala-Hidalgo, and J. J. O'Brien, *The Seasonal Variability of Continental Shelf Circulation in the Northern and Western Gulf of Mexico from a High-Resolution Numerical Model*. American Geophysical Union (AGU), 2005, pp. 203–218.

[31] D. S. Dukhovskoy, E. P. Chassignet, A. Bozec, and S. L. Morey, "Assessment of predictability of the loop current in the gulf of mexico from observing system experiments and observing system simulation experiments," *Frontiers in Marine Science*, vol. 10, 2023.

[32] E. P. Chassignet, H. E. Hurlburt, O. M. Smedstad, G. R. Halliwell, P. J. Hogan, A. J. Wallcraft, R. Baraille, and R. Bleck, "The hycom (hybrid coordinate ocean model) data assimilative system," *Journal of Marine Systems*, vol. 65, no. 1, pp. 60–83, 2007, marine Environmental Monitoring and Prediction.

[33] E. P. Chassignet, H. E. Hurlburt, E. J. Metzger, O. M. Smedstad, J. A. Cummings, G. R. Halliwell, R. Bleck, R. Baraille, A. J. Wallcraft, C. Lozano, H. L. Tolman, A. Srinivasan, S. Hankin, P. Cornillon, R. Weisberg, A. Barth, R. He, F. Werner, and J. Wilkin, "Us godae: Global ocean prediction with the hybrid coordinate ocean model (hycom)," *Oceanography*, vol. 22, no. 2, pp. 64–75, 2009.

[34] E. J. Metzger, O. M. Smedstad, P. G. Thoppil, H. E. Hurlburt, J. A. Cummings, A. J. Wallcraft, L. Zamudio, D. S. Franklin, P. G. Posey, M. W. Phelps, P. J. Hogan, F. L. Bub, and C. J. Dehaan, "US Navy operational global ocean and Arctic ice prediction systems," *Oceanography*, vol. 27, no. 3, pp. 32–43, 2014.

[35] M. Wei, G. Jacobs, C. Rowley, C. N. Barron, P. Hogan, P. Spence, O. M. Smedstad, P. Martin, P. Muscarella, and E. Coelho, "The performance of the us navy's relo ensemble, ncom, hycom during the period of glad at-sea experiment in the gulf of mexico," *Deep Sea Research Part II: Topical Studies in Oceanography*, vol. 129, pp. 374–393, 2016.

[36] B. C. Davis and E. A. McDonald, "Meeting the needs of southeastern coastal resource managers through coastal ocean observing systems," NOAA, SCSGC-T 06-001, 2006.

[37] Z. Xue, J. Zambon, Z. Yao, Y. Liu, and R. He, "An integrated ocean circulation, wave, atmosphere, and marine ecosystem prediction system for the south atlantic bight and gulf of mexico," *Journal of Operational Oceanography*, vol. 8, no. 1, pp. 80–91, 2015.

[38] J. B. Zambon and R. He, "Development of the Coupled Northwest Atlantic Prediction System (CNAPS)," in *American Geophysical Union*, vol. 2016, Feb. 2016, pp. PO14B–2775.

[39] Y. Liu, R. H. Weisberg, L. Zheng, J. Chen, C. Hu, J. Law, and Y. Sun, "Coastal Ocean Response to Hurricane Ian as Simulated by the WFCOM and TBCOM Nowcast/Forecast Systems," in *AGU Fall Meeting Abstracts*, vol. 2022, Dec. 2022, pp. NH43C–05.

[40] A. Srinivasan, T. M. Chin, E. P. Chassignet, M. Iskandarani, and N. Groves, "A statistical interpolation code for ocean analysis and forecasting," *Journal of Atmospheric and Oceanic Technology*, vol. 39, no. 3, pp. 367 – 386, 2022.

[41] P. J. Haley, Jr. and P. F. J. Lermusiaux, "Multiscale two-way embedding schemes for free-surface primitive equations in the "Multidisciplinary Simulation, Estimation and Assimilation System"," *Ocean Dynamics*, vol. 60, no. 6, pp. 1497–1537, Dec. 2010.

[42] P. J. Haley, Jr., A. Agarwal, and P. F. J. Lermusiaux, "Optimizing velocities and transports for complex coastal regions and archipelagos," *Ocean Modeling*, vol. 89, pp. 1–28, 2015.

[43] P. F. J. Lermusiaux and A. R. Robinson, "Data assimilation via Error Subspace Statistical Estimation, part I: Theory and schemes," *Monthly Weather Review*, vol. 127, no. 7, pp. 1385–1407, 1999.

[44] P. F. J. Lermusiaux, "Data assimilation via Error Subspace Statistical Estimation, part II: Mid-Atlantic Bight shelfbreak front simulations, and ESSE validation," *Monthly Weather Review*, vol. 127, no. 7, pp. 1408–1432, Jul. 1999.

[45] P. F. J. Lermusiaux, C. Mirabito, P. J. Haley, Jr., W. H. Ali, A. Gupta, S. Jana, E. Dorfman, A. Laferriere, A. Kofford, G. Shepard, M. Goldsmith, K. Heaney, E. Coelho, J. Boyle, J. Murray, L. Freitag, and A. Morozov, "Real-time probabilistic coupled ocean physics-acoustics forecasting and data assimilation for underwater GPS," in *OCEANS 2020 IEEE/MTS*. IEEE, Oct. 2020, pp. 1–9.

[46] W. G. Leslie, A. R. Robinson, P. J. Haley, Jr, O. Logutov, P. A. Moreno, P. F. J. Lermusiaux, and E. Coelho, "Verification and training of real-time forecasting of multi-scale ocean dynamics for maritime rapid environmental assessment," *Journal of Marine Systems*, vol. 69, no. 1, pp. 3–16, 2008.

[47] P. J. Haley, Jr., P. F. J. Lermusiaux, A. R. Robinson, W. G. Leslie, O. Logoutov, G. Cossarini, X. S. Liang, P. Moreno, S. R. Ramp, J. D. Doyle, J. Bellingham, F. Chavez, and S. Johnston, "Forecasting and reanalysis in the Monterey Bay/California Current region for the Autonomous Ocean Sampling Network-II experiment," *Deep Sea Research Part II: Topical Studies in Oceanography*, vol. 56, no. 3–5, pp. 127–148, Feb. 2009.

[48] P. F. J. Lermusiaux, D. N. Subramani, J. Lin, C. S. Kulkarni, A. Gupta, A. Dutt, T. Lolla, P. J. Haley, Jr., W. H. Ali, C. Mirabito, and S. Jana, "A future for intelligent autonomous ocean observing systems," *Journal of Marine Research*, vol. 75, no. 6, pp. 765–813, Nov. 2017, the Sea. Volume 17, The Science of Ocean Prediction, Part 2.

[49] D. N. Subramani, P. J. Haley, Jr., and P. F. J. Lermusiaux, "Energy-optimal path planning in the coastal ocean," *Journal of Geophysical Research: Oceans*, vol. 122, pp. 3981–4003, 2017.

[50] C. S. Kulkarni, P. J. Haley, Jr., P. F. J. Lermusiaux, A. Dutt, A. Gupta, C. Mirabito, D. N. Subramani, S. Jana, W. H. Ali, T. Peacock, C. M. Royo, A. Rzeznik, and R. Supekar, "Real-time sediment plume modeling in the Southern California Bight," in *OCEANS Conference 2018*. Charleston, SC: IEEE, Oct. 2018.

[51] A. Gupta, P. J. Haley, D. N. Subramani, and P. F. J. Lermusiaux, "Fish modeling and Bayesian learning for the Lakshadweep Islands," in *OCEANS 2019 MTS/IEEE SEATTLE*. Seattle: IEEE, Oct. 2019, pp. 1–10.

[52] P. F. J. Lermusiaux, M. Doshi, C. S. Kulkarni, A. Gupta, P. J. Haley, Jr., C. Mirabito, F. Trotta, S. J. Levang, G. R. Flierl, J. Marshall, T. Peacock, and C. Noble, "Plastic pollution in the coastal oceans: Characterization and modeling," in *OCEANS 2019 MTS/IEEE SEATTLE*. Seattle: IEEE, Oct. 2019, pp. 1–10.

[53] P. F. J. Lermusiaux, D. G. M. Anderson, and C. J. Lozano, "On the mapping of multivariate geophysical fields: Error and variability subspace estimates," *Quarterly Journal of the Royal Meteorological Society*, vol. 126, no. 565, pp. 1387–1429, 2000.

[54] P. F. J. Lermusiaux, "On the mapping of multivariate geophysical fields: Sensitivities to size, scales, and dynamics," *Journal of Atmospheric and Oceanic Technology*, vol. 19, no. 10, pp. 1602–1637, 2002.

[55] O. G. Logutov and P. F. J. Lermusiaux, "Inverse barotropic tidal estimation for regional ocean applications," *Ocean Modelling*, vol. 25, no. 1–2, pp. 17–34, 2008. [Online]. Available: http://www.sciencedirect.com/science/article/pii/S1463500308000851

[56] A. Agarwal and P. F. J. Lermusiaux, "Statistical field estimation for complex coastal regions and archipelagos," *Ocean Mod-*

elling, vol. 40, no. 2, pp. 164–189, 2011.
[57] P. F. J. Lermusiaux, "Evolving the subspace of the three-dimensional multiscale ocean variability: Massachusetts Bay," *Journal of Marine Systems*, vol. 29, no. 1, pp. 385–422, 2001.
[58] P. F. J. Lermusiaux, "Uncertainty estimation and prediction for interdisciplinary ocean dynamics," *Journal of Computational Physics*, vol. 217, no. 1, pp. 176–199, 2006.
[59] P. F. J. Lermusiaux, "Estimation and study of mesoscale variability in the Strait of Sicily," *Dynamics of Atmospheres and Oceans*, vol. 29, no. 2, pp. 255–303, 1999.
[60] P. F. J. Lermusiaux, "Adaptive modeling, adaptive data assimilation and adaptive sampling," *Physica D: Nonlinear Phenomena*, vol. 230, no. 1, pp. 172–196, 2007.
[61] P. F. J. Lermusiaux, T. Lolla, P. J. Haley, Jr., K. Yigit, M. P. Ueckermann, T. Sondergaard, and W. G. Leslie, "Science of autonomy: Time-optimal path planning and adaptive sampling for swarms of ocean vehicles," in *Springer Handbook of Ocean Engineering: Autonomous Ocean Vehicles, Subsystems and Control*, T. Curtin, Ed. Springer, 2016, ch. 21, pp. 481–498.
[62] P. F. J. Lermusiaux, P. J. Haley, Jr, and N. K. Yilmaz, "Environmental prediction, path planning and adaptive sampling: sensing and modeling for efficient ocean monitoring, management and pollution control," *Sea Technology*, vol. 48, no. 9, pp. 35–38, 2007.
[63] C. J. Olson, J. J. Becker, and D. T. Sandwell, "A new global bathymetry map at 15 arcsecond resolution for resolving seafloor fabric: SRTM15_PLUS," in *AGU Fall Meeting*. San Francisco: American Geophysical Union, Dec. 2014, pp. OS34A–03.
[64] ——, "SRTM15_PLUS: Data fusion of Shuttle Radar Topography Mission (SRTM) land topography with measured and estimated seafloor topography," Dataset, May 2016, NCEI Accession 0150537.
[65] B. Tozer, D. T. Sandwell, W. H. F. Smith, C. Olson, J. R. Beale, and P. Wessel, "Global bathymetry and topography at 15 arc sec: SRTM15+," *Earth and Space Science*, vol. 6, no. 10, pp. 1847–1864, Oct. 2019.
[66] G. D. Egbert and S. Y. Erofeeva, "Efficient inverse modeling of barotropic ocean tides," *Journal of Atmospheric and Oceanic Technology*, vol. 19, no. 2, pp. 183–204, 2002.
[67] ——, "OSU tidal inversion," 2013. [Online]. Available: http://volkov.oce.orst.edu/tides/tpxo8_atlas.html
[68] National Centers for Environmental Prediction (NCEP), "Climate Forecast System (CFS)," Jul. 2023. [Online]. Available: https://www.ncei.noaa.gov/products/weather-climate-models/climate-forecast-system
[69] J. A. Cummings and O. M. Smedstad, *Variational Data Assimilation for the Global Ocean*. Berlin, Heidelberg: Springer Berlin Heidelberg, 2013, pp. 303–343.
[70] The HYCOM Consortium, "HYbrid Coordinate Ocean Model (HYCOM)," Jul. 2023, accessed 2019-04-09. [Online]. Available: https://hycom.org
[71] National Centers for Environmental Prediction (NCEP), "Global Forecast System (GFS)," Jul. 2023, Accessed 2019-04-09. [Online]. Available: https://www.emc.ncep.noaa.gov/index.php?branch=GFS
[72] Copernicus Climate Change Service (C3S), "ERA5 hourly data on single levels from 1940 to present," Copernicus Climate Change Service (C3S) Climate Data Store (CDS), Jul. 2023, Accessed 2023-07-29.
[73] H. Hersbach, B. Bell, P. Berrisford, G. Biavati, A. Horányi, J. Muñoz Sabater, J. Nicolas, C. Peubey, R. Radu, I. Rozum, D. Schepers, A. Simmons, C. Soci, D. Dee, and J.-N. Thépaut, "ERA5 hourly data on single levels from 1940 to present," Copernicus Climate Change Service (C3S) Climate Data Store (CDS), Jul. 2023, Accessed 2023-07-29.
[74] MITgcm, "Massachusetts Institute of Technology General Circulation Model," Jul. 2023, accessed 2023-07-29. [Online]. Available: https://mitgcm.org/
[75] H. G. Arango and A. F. Shchepetkin, "Regional Ocean Modeling System," Jul. 2023, accessed 2023-07-29. [Online]. Available: https://www.myroms.org/
[76] G. Madec and the NEMO System Team, "NEMO ocean engine reference manual," Zenodo, Jul. 2023.
[77] P. F. J. Lermusiaux, A. J. Miller, and N. Pinardi, "Special issue of Dynamics of Atmospheres and Oceans in honor of Prof. A. R. Robinson," *Dynamics of Atmospheres and Oceans*, vol. 52, no. 1–2, pp. 1–3, Sep. 2011, Editorial.
[78] P. F. J. Lermusiaux, P. Malanotte-Rizzoli, D. Stammer, J. Carton, J. Cummings, and A. M. Moore, "Progress and prospects of U.S. data assimilation in ocean research," *Oceanography*, vol. 19, no. 1, pp. 172–183, 2006.
[79] P. F. J. Lermusiaux, P. J. Haley, Jr., S. Jana, A. Gupta, C. S. Kulkarni, C. Mirabito, W. H. Ali, D. N. Subramani, A. Dutt, J. Lin, A. Shcherbina, C. Lee, and A. Gangopadhyay, "Optimal planning and sampling predictions for autonomous and Lagrangian platforms and sensors in the northern Arabian Sea," *Oceanography*, vol. 30, no. 2, pp. 172–185, Jun. 2017, special issue on Autonomous and Lagrangian Platforms and Sensors (ALPS).
[80] T. P. Boyer, O. K. Baranova, C. Coleman, H. E. Garcia, A. Grodsky, R. A. Locarnini, A. V. Mishonov, C. R. Paver, J. R. Reagan, D. Seidov, I. V. Smolyar, K. W. Weathers, and M. M. Zweng, *World Ocean Database 2018*, NOAA, Silver Spring, MD, Sep. 2018.
[81] T. M. Cover, *Elements of information theory*. John Wiley & Sons, 1999.
[82] A. K. Nickerson, R. H. Weisberg, and Y. Liu, "On the evolution of the gulf of mexico loop current through its penetrative, ring shedding and retracted states," *Advances in Space Research*, vol. 69, no. 11, pp. 4058–4077, 2022.
[83] National Oceanographic and Atmospheric Administration and Atlantic Oceanographic and Meteorological Laboratory, "NOAA/AOML altimetry-derived products," Jul. 2023, Accessed 2023-07-30.
[84] M. Andres, "Variability at multiple scales: Using an array of current- and pressure-sensor equipped inverted echo sounders to measure the ocean," Defense Technical Information Center, Tech. Rep. AD1023122, 2008.
[85] Argo, "Argo float data and metadata from Global Data Assembly Centre (Argo GDAC)," 2000.
[86] R. H. Weisberg, "Observations at the West Florida Shelf Pressure Point: How the Pressure Point affects both the Shelf and the Gulf of Mexico Loop Current," PowerPoint slides, Aug. 2020. [Online]. Available: https://secoora.org/wp-content/uploads/2020/08/RHW8-25-20.pdf
[87] GCOOS: Gulf of Mexico Ocean Observing System, "Stones Metocean observatory project," Jul. 2023. [Online]. Available: https://gcoos.org/stones
[88] U.S. Integrated Ocean Observing System, "HF radar: History," Jul. 2023. [Online]. Available: https://ioos.noaa.gov/project/hf-radar/